Showcasing collaborative research from Taiki Hoshino group, International Center for Synchrotron Radiation Innovation Smart (SRIS), Tohoku University, and from Professor Takashi Kato group, Department of Chemistry and Biotechnology, School of Engineering, The University of Tokyo.

Experimental probing of dynamic self-organized columnar assemblies in colloidal liquid crystals

The authors experimentally unveiled the static structures and dynamical behavior in columnar colloidal liquid crystals through X-ray photon correlation spectroscopy measurements using refined model samples. These new colloidal liquid crystals were formed by assembly of hybrid platelike nanoparticles prepared with biomineralization-inspired methods. This research will contribute to better understanding of molecular assemblies and colloidal systems, as well as the design of self-assembled materials.

As featured in:

ROYAL SOCIETY
OF **CHEMISTRY**

rsc.li/nanoscale-advances

ROYAL SOCIETY
OF CHEMISTRY

Experimental probing of dynamic self-organized columnar assemblies in colloidal liquid crystals†

Taiki Hoshino, ‡*[abc] Masanari Nakayama, ‡*[d] Yoshihiro Hosokawa,[d] Kohei Mochizuki,[d] Satoshi Kajiyama, [d] Yoshiki Kohmura[b] and Takashi Kato [*de]

Self-organized supramolecular assemblies are widespread in nature and technology in the form of liquid crystals, colloids, and gels. The reversible nature of non-covalent bonding leads to dynamic functions such as stimuli-responsive switching and self-healing, which are unachievable from an isolated molecule. However, multiple intermolecular interactions generate diverse conformational and configurational molecular motions over various time scales in their self-assembled states, and their specific dynamics remains unclear. In the present study, we have experimentally unveiled the static structures and dynamical behaviors in columnar colloidal liquid crystals by a coherent X-ray scattering technique using refined model samples. We have found that controlling the size distribution of the colloidal nanoplates dramatically changed their static and dynamic properties. Furthermore, the resulting dynamical behaviors obtained by X-ray photon correlation spectroscopy have been successfully decomposed into multiple distinct modes, allowing us to explore the dynamical origin in the colloidal liquid-crystalline state. The present approaches using a columnar liquid crystal may contribute to a better understanding of the dynamic nature of molecular assemblies and dense colloidal systems and bring valuable insights into rational design of functional properties of self-assembled materials such as stimuli-responsive liquid crystals, self-healing gels, and colloidal crystals. For these materials, the motion of constituent particles and molecules in the self-assembled state is a key factor for structural formation and dynamically responsive performance.

1 Introduction

For self-assembled materials such as liquid crystals, a variety of molecules or particles spontaneously organize into ordered assemblies.[1–7] They show dynamical and responsive functions that cannot be obtained from a single molecular component. A colloidal liquid crystal is one of the self-assembled functional materials.[7–12] The components with anisotropic shapes of particles form ordered and mobile assembled states. Recently we reported that biomineralization-inspired colloidal liquid crystals were formed based on calcium carbonate $(CaCO_3)$[13,14] and hydroxyapatite[15–18] particles complexed with an acidic

aInternational Center for Synchrotron Radiation Innovation Smart (SRIS), Tohoku University, 2-1-1 Katahira, Aoba-ku, Sendai 980-8577, Japan. E-mail: taiki.hoshino. c7@tohoku.ac.jp

bRIKEN SPring-8 Center, 1-1-1, Kouto, Sayo-cho, Sayo-gun, Hyogo 679-5148, Japan

cInstitute of Multidisciplinary Research for Advanced Materials (IMRAM), Tohoku University, 2-1-1 Katahira, Aoba-ku, Sendai 980-8577, Japan

dDepartment of Chemistry and Biotechnology, School of Engineering, The University of Tokyo, 7-3-1, Hongo, Bunkyo-ku, Tokyo 113-8656, Japan. E-mail: masanarinakayama@gmail.com; kato@chiral.t.u-tokyo.ac.jp

eResearch Initiative for Supra-Materials, Shinshu University, 4-17-1, Wakasato, Nagano, Japan

† Electronic supplementary information (ESI) available. See DOI: https://doi.org/10.1039/d3na00183k

‡ Equal contribution.

macromolecule, poly(acrylic acid) (PAA). For hydroxyapatite-based liquid crystals, stimuli responsive properties and bio-functions, *e.g.*, magnetic field responsive colloidal liquid crystals composed of nanorods, were reported.[16,18,19]

There has been an attractive challenge of capturing the dynamic nature of functional self-organized soft materials for designing their material applications. For further functionalization of these colloidal nanorod liquid crystals, it is important to understand the dynamic nature of the materials in their self-organized states. Our intention is to examine the dynamic behaviors of colloidal columnar liquid-crystalline (LC) phases displayed by plate-like nanoparticles in aqueous solution. X-ray photon correlation spectroscopy (XPCS) is a powerful technique for probing the dynamics of opaque concentrated colloidal systems and heterogeneous dynamics on a wide range of spatial scales by analyzing the temporal fluctuations of the scattered speckles obtained by partially coherent X-ray scattering.[20–27] We previously studied the behavior of nematic colloidal liquid crystals formed by biomineral-based rod-like hybrids by XPCS.[28] We observed that they exhibited faster dynamics in the direction of the director than in the perpendicular direction in the LC phase when kept for a long period.

Simulation studies on colloidal liquid crystals suggested that the dynamics of rod-like and plate-like particles are quite different.[29–31] The diffusion in the direction parallel to the

nematic director is faster than the diffusion in the direction perpendicular to the director in rod-like particles in the liquid crystal colloid phase, while the opposite tendency can appear in plate-like liquid crystal colloids. Experimental studies on dynamics of rod-like colloids in LC phases were performed;[28,32–34] however, the dynamics of plate-like colloids were only studied for isotropic and lamellar phases.[35–37] The experimental measurement for the columnar colloidal liquid crystals composed of plate-like particles has not yet been performed. It is expected that the dynamical behavior of well-controlled plate-like colloids in the LC phase can provide significant information for understanding colloidal dynamic properties.

Here, we report new colloidal liquid crystals formed by biomineralization-inspired hybrid plate-like nanoparticles and their dynamical properties using XPCS (Fig. 1). We also show that acidic molecules of sodium dodecyl sulfonate (SDS) and

PAA are available as a new synthetic template mixture for the preparation of colloidal $CaCO_3$ nanoplates (Fig. 1a).

2 Results and discussion

We have developed a biomineralization-inspired method for synthesizing $CaCO_3$ nanoplates (Fig. 1a). Furthermore, narrow-disperse nanoplates were fractionated from wide-disperse nanoplates by centrifugation processes, and the static structures and dynamical behavior were characterized using X-ray scattering measurements (Fig. 1b).

2.1 Synthesis of nanoplates

The nanoplates were obtained by crystal growth of $CaCO_3$ in new bilayer templates. The procedure for preparing templates using SDS and PAA molecules and subsequently synthesizing nanoplates is shown below.

In the initial synthetic procedure, SDS and PAA molecules were dissolved in an aqueous $CaCl_2$ solution. The electrostatic interactions among these molecular components and Ca^{2+} ions resulted in the formation of layered structures of Ca^{2+} ions covered with dodecyl sulfonate (DS^-) bilayers that functioned as a template for two-dimensional (2D) crystal growth of $CaCO_3$. The 2D morphologies of layered templates were confirmed by scanning electron microscopy (SEM) observation (Fig. S1†). The X-ray diffraction (XRD) measurements of the layered templates revealed an interlayer distance of 30.1 Å, which was consistent with the value previously reported (Fig. S2†).[38] On the other hand, no change of the interlayer distance was observed by varying the concentration of PAA in the XRD patterns (Fig. S2†), which suggests that PAA molecules existed outside the templates. Thermogravimetric (TG) analysis showed the presence of organic compounds together with Ca^{2+} ions in the template (Fig. S3†), and energy-dispersive X-ray spectroscopy (EDS) analysis revealed a $1:2$ molar ratio of Ca^{2+} ions to sulfonate groups (Fig. S4†), which is well in accordance with the layered structures.

The addition of Na_2CO_3 after template formation was expected to induce dissociation of a part of the DS^- molecules from the Ca^{2+} ions in the template and replacement with the CO_3^{2-} ions, which induced the crystallization of $CaCO_3$. We also expected the residual DS^- molecules to act as a template for 2D crystal growth. In the time course of crystallization tracked by XRD measurements and Fourier-transform infrared (FTIR) spectroscopy (Fig. S5†), the peaks attributed to calcium dodecyl sulfonate crystals were observed before the addition of Na_2CO_3, whereas the peaks characteristic of calcite, which is a polymorph of $CaCO_3$ crystals, appeared 1 h after the addition of Na_2CO_3. In 72 h, only the peaks for calcite crystals were identified, which shows that the crystal growth of $CaCO_3$ was completed in the templates.

Fig. 2 shows the SDS concentration dependence of the morphology of the precipitates at a PAA concentration of 0.14 wt%, which was observed by SEM. When the SDS concentration was over 80 mM, plate-like crystals were obtained. For a concentration below 80 mM, no plate-like particles but thick
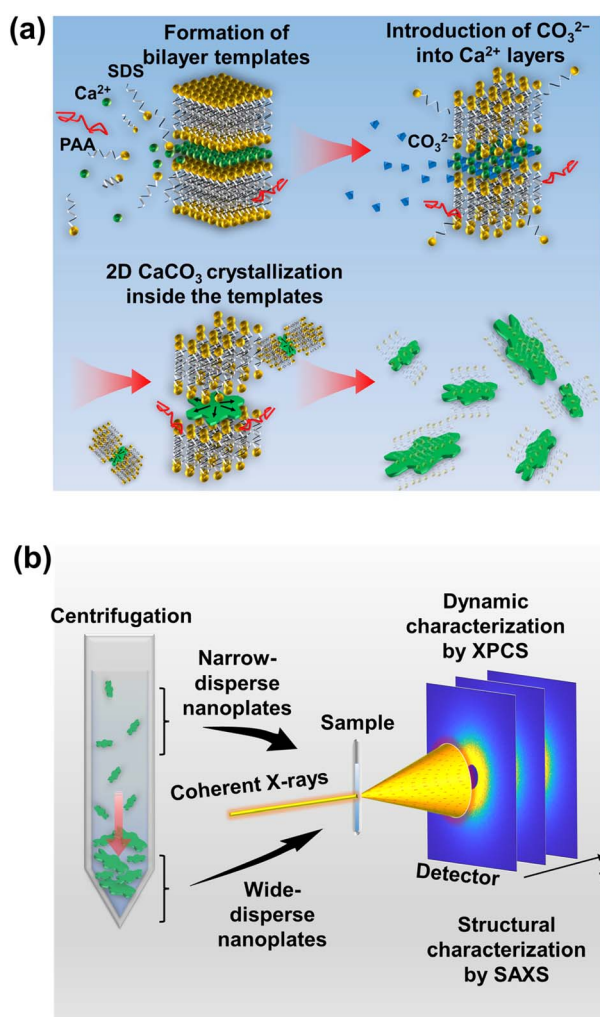

Fig. 1 Schematic illustration of the synthesis of a columnar colloidal liquid crystal and characterization. (a) Synthetic approach towards $CaCO_3$ nanoplates using organic templates combining SDS and PAA molecules inspired by biomineralization. (b) Size fractionation of narrow-disperse nanoplates from wide-disperse nanoplates by centrifugation and characterization using X-ray scattering techniques.
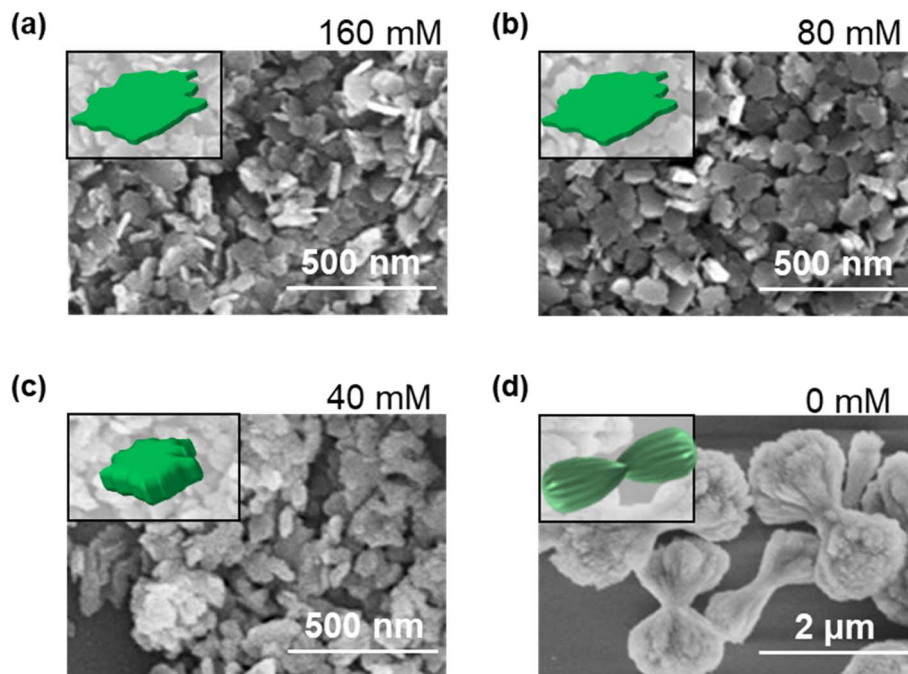
Fig. 2 SEM images of precipitates prepared at different SDS concentrations of (a) 160 mM, (b) 80 mM, (c) 40 mM, and (d) 0 mM with the corresponding shape illustrations. All the precipitates were obtained at a PAA concentration of 0.14 wt%.

aggregates and dumbbell-shaped crystals were formed due to the absence of 2D templates. The effects of the concentration of PAA were examined as shown in Fig. S6,† the SEM images of the precipitates at an SDS concentration of 80 mM. In the absence of PAA, larger plates were formed (Fig. S6a†), which suggests that PAA molecules suppressed excessive crystal growth of $CaCO_3$ and imparted a uniformity in the particle size. When the PAA concentration increased from 0.14 to 0.29 wt%, no defined crystal morphologies were observed (Fig. S6c†) probably because PAA interfered with DS^- binding with Ca^{2+} ions, and inhibited the formation of 2D templates. The inorganic/organic composite structures of nanoplates were examined by TG analysis. Organic compounds and $CaCO_3$ decomposed at around 200 and 600 °C, respectively, and the weight fraction of organic components in the template was estimated to be 11.4 wt% (Fig. S7†). The EDS analysis revealed a molar ratio of Ca^{2+} ions to sulfonate groups of 1 : 0.04 in the nanoplate particles (Fig. S8†). This ratio means that 4.84 DS^- molecules per 1 nm^2 were adsorbed on the surfaces of the nanoplates. The dense DS^- molecules can form bilayers on the nanoplate surfaces. Indeed, the zeta potential of the particle surfaces was -23.4 ± 6 mV, and the negative electrostatic forces stabilized colloidal dispersion (Fig. S9†).

Tuning the SDS concentration to 80 mM and the PAA concentration to 0.14 wt%, we have successfully achieved the synthesis of plate-like $CaCO_3$ crystals as shown in the SEM image in Fig. 3a. The $CaCO_3$ nanocrystals affected by the organic matrix exhibit thin nanoplate morphologies. In the synthetic processes, SDS and PAA played significant roles in the morphological control of the $CaCO_3$ nanoplates. Although the shape of the nanoplates was inhomogeneous, the maximum

widths and the thicknesses were estimated to be 118 ± 40 nm and 17.4 ± 3.5 nm, respectively, based on the SEM observations (Fig. 3b and c). The relative standard deviations of the maximum width σ_w and the thickness σ_t were 34% and 20%, respectively. The nanoplates had a broad width distribution and were named as wide-disperse nanoplates. If nanoplates with a narrower size distribution were obtained, deeper analysis of the structure and dynamical behavior would be expected. By further centrifuging the supernatant of the wide-disperse nanoplates, nanoplates with a narrower width distribution were fractionated (Fig. 3d), and were named narrow-disperse nanoplates. In this case, the maximum widths and the thicknesses were estimated to be 97 ± 22 nm and 14.9 ± 3.7 nm, respectively (Fig. 3e and f) and the relative standard deviations of the maximum width σ_w and the thickness σ_t were 23 and 25%, respectively, indicative of the significant reduction in the polydispersity of the maximum width compared with that of wide-disperse nanoplates. The polydispersity changes were also observed as the difference in optical transparency for the colloidal dispersions of wide-disperse and narrow-disperse nanoplates (Fig. S10†).

2.2 Static and dynamic characterization by X-ray scattering measurements

The self-assembly of dispersed nanoplates resulted in the formation of specific morphologies. While forming a specific morphology, the nanoplates are not completely stationary, but dynamically fluctuate due to the thermal motion of the solvent molecules. Both static structures and dynamic properties are important for their functional properties. To investigate these properties, we conducted coherent X-ray scattering
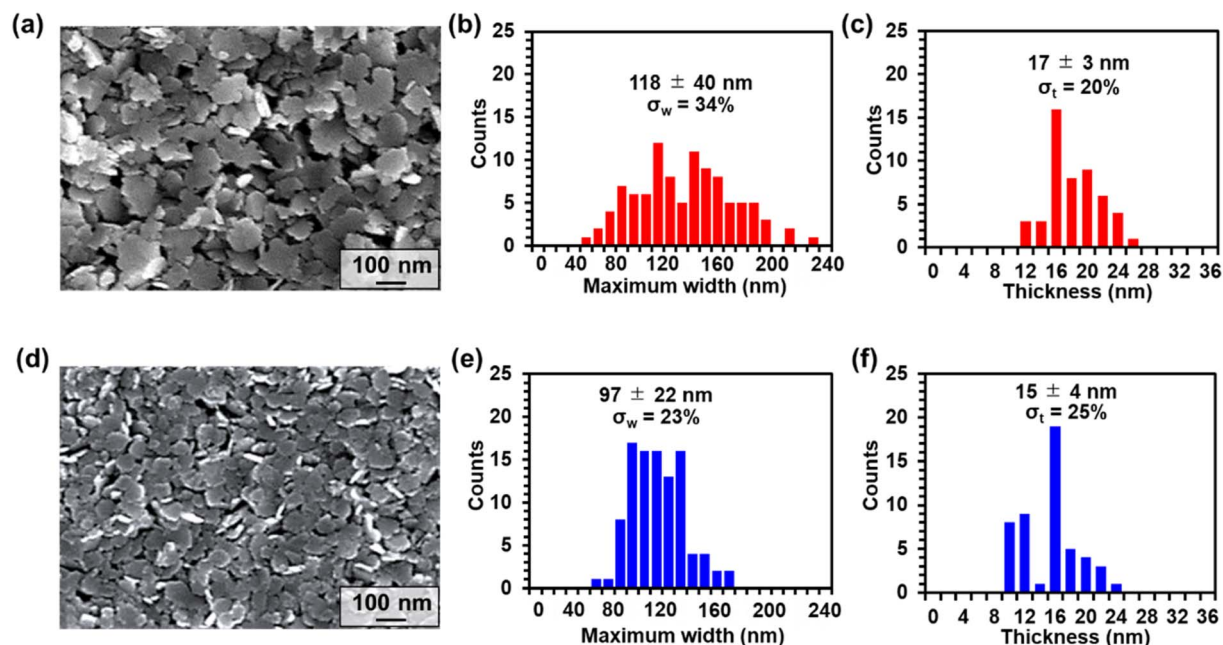
Fig. 3 Characterization of wide-disperse nanoplates in comparison with narrow-disperse nanoplates. (a) and (d) SEM images of (a) wide-disperse and (d) narrow-disperse nanoplates after size fractionation. (b) and (e) The histograms for the maximum widths and (c) and (f) thicknesses of (b) and (c) wide-disperse and (e) and (f) narrow-disperse nanoplates.

measurements in the small-angle X-ray scattering (SAXS) geometry (see Section 4.3 for details). This setup enabled us to analyze both the static structure and dynamic properties under the same conditions. By analyzing scattering images obtained from a certain exposure time, we could evaluate the static structures through SAXS profiles. Meanwhile, we performed XPCS analysis on the fluctuations of scattering images obtained through time-resolved measurements to evaluate dynamics.

2.2.1 SAXS measurements of the colloidal LC structures. The self-assembly of wide-disperse and narrow-disperse nanoplates into colloidal solutions was investigated by polarizing optical microscope (POM) (Fig. 4) and SAXS measurements
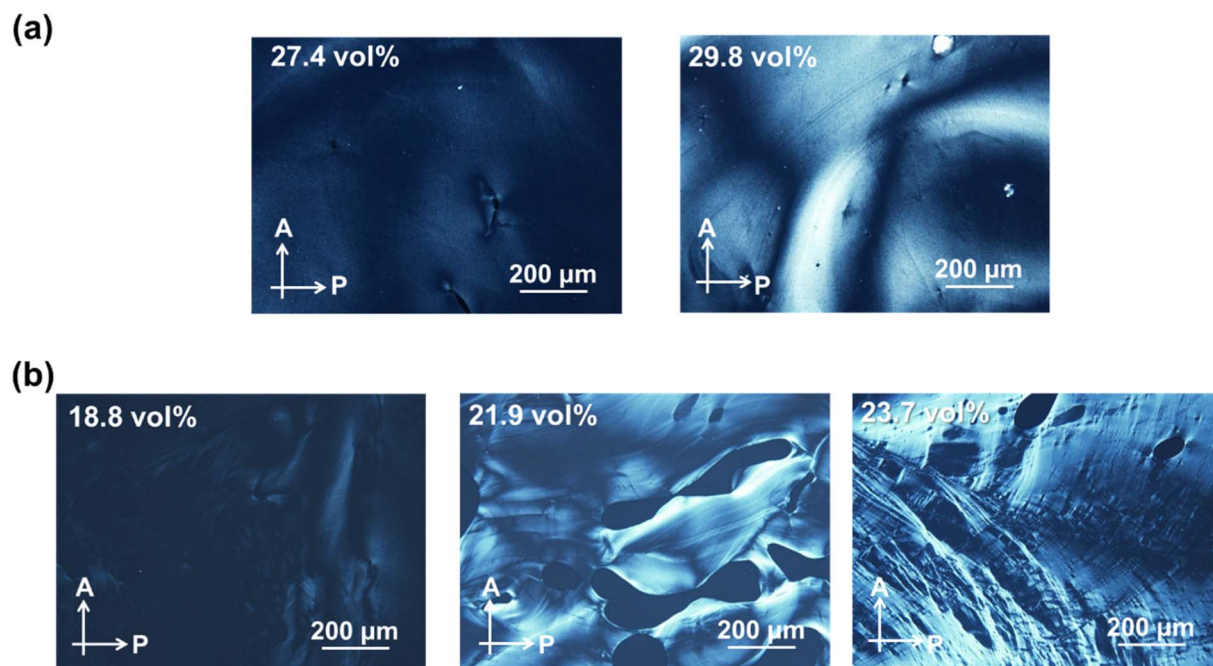

Fig. 4 POM images of colloidal dispersions of (a) wide-disperse nanoplates at different concentrations of 27.4 vol% and 29.8 vol%, and (b) narrow-disperse nanoplates at different concentrations of 18.8 vol%, 21.9 vol% and 23.7 vol%. A: analyzer; P: polarizer.
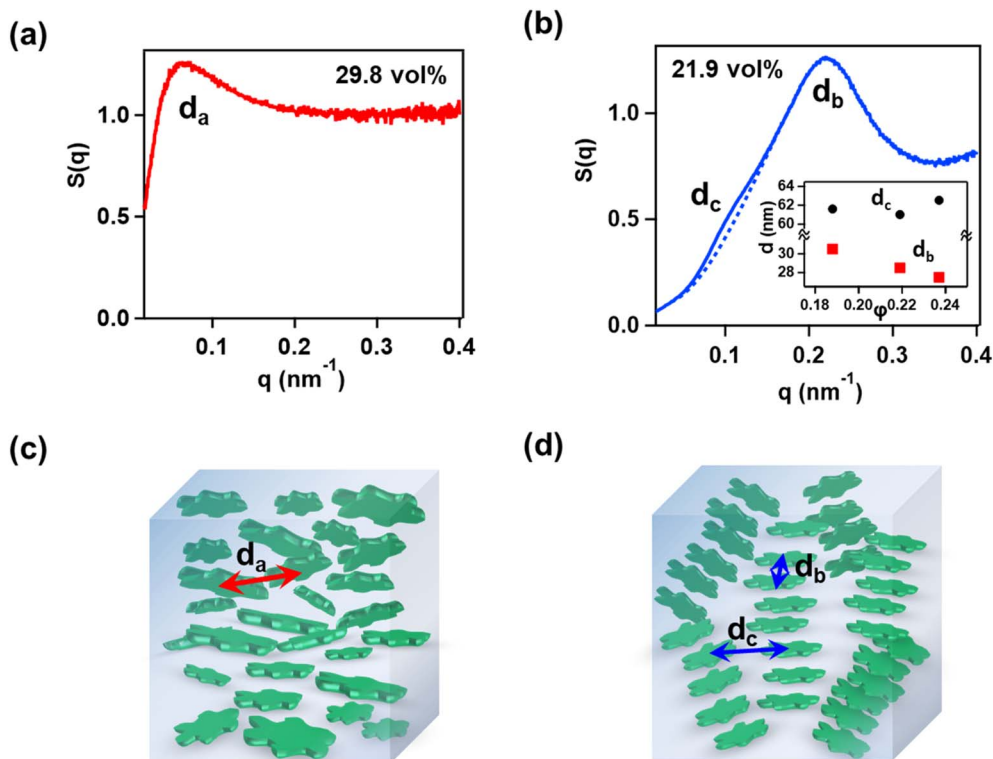
Fig. 5 (a) and (b) Structure factors $S(q)$ of colloidal dispersions of (a) wide–disperse nanoplates at 29.8 vol% and (b) narrow–disperse nanoplates at 21.9 vol% with a fitted baseline at around $q = 0.1$ nm^{-1}. The inset presents the concentration (φ) dependences of correlation lengths. (c) and (d) Schematic illustrations of the self-assembled LC states of (c) wide–disperse and (d) narrow–disperse nanoplates in the colloidal dispersions at 29.8 vol% and 21.9 vol%, respectively, with the correlation lengths d_a, d_b, and d_c estimated from the peak of $S(q)$.

(Fig. 5, S11 and S12†). In the POM observations in their dilute colloidal dispersions, fluidic birefringence was partially observed at a concentration of 27.4 vol% for wide-disperse nanoplates and at a concentration of 18.8 vol% for narrow-disperse nanoplates, respectively. These observations show that nanoplates gained orientational orders in their concentrated colloidal dispersions, forming coexisting isotropic/LC phases. LC textures were observed in the whole area at higher concentrations over 29.8 vol% and 21.9 vol% for the wide-disperse and narrow-disperse nanoplates, respectively, indicative of the formation of homogeneous LC phases.

In the SAXS measurements, isotropic 2D images were obtained at all the measured concentrations for both wide-disperse and narrow-disperse nanoplates (Fig. S11a and S12a†). It indicates that even in the LC phase, the domain size is sufficiently smaller than the X-ray irradiation volume (ca. $0.02 \times 0.02 \times 2$ mm^3). The intensity profiles $I(q)$, where q is the scattering vector, showed differences between wide-disperse and narrow-disperse nanoplates (Fig. S11b and S12b†). The structure factor $S(q)$ can be obtained by dividing $I(q)$ by that for the diluted dispersion (Fig. S11c and S12c†). The representative $S(q)$ for wide-disperse nanoplates at 29.8 vol% and narrow-disperse nanoplates at 21.9 vol% is shown in Fig. 5a and b, respectively. $S(q)$ for the wide-disperse nanoplates has only one peak at $q = 0.067$ nm^{-1}. This suggests that the LC phase of the wide-disperse nanoplates was a discotic nematic (N_D) phase, with

an average interparticle distance (d_a) of 94 nm as schematically shown in Fig. 5c. On the other hand, for the narrow-disperse nanoplates, $S(q)$ has a peak and a shoulder at different q values of around 0.220 nm^{-1} and 0.103 nm^{-1}, respectively. This suggests that the LC phase of narrow-disperse nanoplates was a columnar nematic (N_C) phase, with an intra-columnar distance (d_b) of 29 nm and an inter-columnar distance (d_c) of 61 nm as schematically shown in Fig. 5d.[39–41] Reasonably, the intra-columnar and inter-columnar distances were larger than the thickness and the minimum width of the nanoplates, respectively. d_b decreased on increasing the concentration although d_c had no clear concentration dependence (Fig. 5b inset). The lack of a clear concentration dependence of d_c can be due to the inhomogeneous in-plane morphologies of the nanoplates.

Similar SAXS profiles suggesting two short-range orders were previously observed in columnar nematic phases for plate-like particles such as Al(OH)$_3$ nanoplates,[39] Sb$_3$P$_2$O$_{14}$$^{3-}$ nanosheets,[40] and CeF$_3$ nanodisks.[42] A Schlieren texture similar to that in Fig. 4b was also observed by POM in a columnar nematic phase of lyotropic discotic liquid crystals.[43] These previous reports support the presence of the columnar nematic phase for narrow-disperse nanoplates, which were analyzed combining POM and SAXS.

2.2.2 XPCS measurements of colloidal liquid crystals. The dynamical behavior of the colloidal liquid crystals was studied

by XPCS measurements. In the XPCS measurements, the fluctuation of the scattering intensity $I(\boldsymbol{q}, t)$ at a scattering vector $\boldsymbol{q}$ was obtained over a time series t, and the intensity time autocorrelation function was calculated as

$$g_2(\boldsymbol{q}, t) = \langle I(\boldsymbol{q}, t')I(\boldsymbol{q}, t' + t)\rangle/\langle I(\boldsymbol{q}, t')\rangle^2, \tag{1}$$

where $q = |\boldsymbol{q}|$ and the angle brackets indicate time averaging. Fig. 6a shows g_2 at $q = 0.0426$ nm^{-1} as representative data for the colloidal dispersions of wide-disperse nanoplates at different concentrations of 27.4 and 29.8 vol%. All the measured g_2 were well expressed with the following expression

$$g_2(q, t) = \beta \exp\left[-2(\Gamma t)^{\alpha}\right] + 1, \tag{2}$$

where β is the speckle contrast ($\sim$0.05–0.06) determined by the experimental condition, and Γ and α are the relaxation rate and stretched exponent ($\alpha < 1$), respectively. The obtained Γ and α show no clear concentration and q dependence (Fig. S13†). The N_D phase formed from wide-disperse nanoplates showed extremely stretched relaxations, probably due to the size polydispersity and the less ordered structure.

Fig. 6b shows the plots of g_2 at $q = 0.0426$ nm^{-1} as representative data for the colloidal dispersions of narrow-disperse nanoplates at different concentrations of 18.8, 21.9, and 23.7 vol%. The relaxation slowed down on increasing the concentration. The significant slowdown on increasing the concentration, despite the small change in the interparticle distance, is a similar feature to that of our previously reported nanorod colloidal liquid crystals.[28] Focusing on g_2 at 23.7 vol%, inflection points that indicate the existence of several relaxation modes were found, rather than extremely stretched relaxation as observed in the wide-disperse systems. Therefore, we performed Laplace transform analysis to decompose the relaxation modes. The Siegert relationship relates g_2 to the intermediate scattering function g_1,[44]

$$g_2(q, t) = \beta[g_1(q, t)]^2 + 1. \tag{3}$$

We performed the Laplace transform *via* CONTIN analysis for the experimentally obtained g_2.[45] In the analysis, g_1 was expressed by using the following function with a continuous distribution of $\exp(-\gamma t)$ given by

$$g_1(q, t) = A\int H(q, \gamma)\exp(-\gamma t)\mathrm{d}\gamma, \tag{4}$$

where A is a constant value and $H(q, \gamma)$ is the spectral density function. As shown in Fig. 6c, the number of peaks in $H(q, \gamma)$ transformed from g_2 at $q = 0.0426$ nm^{-1} increased from one to three on increasing the concentration from 18.8 vol% to 23.7 vol%. The concentration dependence on the peak number was common in all the other measured q ranges.

Based on the results of the Laplace transform analysis, we performed the fitting analysis by substituting the following g_1 into eqn (3),

$$g_1(q, t) = \sum_{i=1}^{p} C_i \exp\left[-(\Gamma_i t)^{\alpha_i}\right] \tag{5}$$

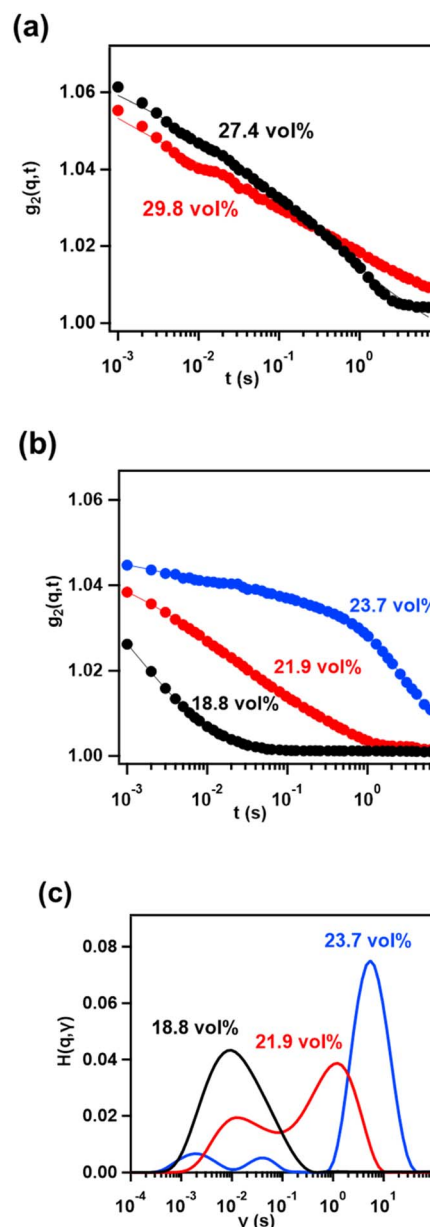**Fig. 6** (a) and (b) Time autocorrelation functions $g_2(q, t)$ at $q = 0.0426$ nm^{-1} for the colloidal dispersions of wide-disperse nanoplates at different concentrations of 27.4 vol% and 29.8 vol% (a), and narrow-disperse nanoplates at different concentrations of 18.8 vol%, 21.9 vol% and 23.7 vol% (b). (c) Laplace transform of the $g_2(q, t)$ for the colloidal dispersions of narrow-disperse nanoplates at different concentrations.

where C_i is the constant value, Γ_i is the relaxation rate, α_i is the stretched or compressed exponent, and $i = 1, 2,$ and 3 represents the number of individual dynamics in the order from the slowest to the fastest rate at each concentration, respectively.

The obtained q dependences of Γ_i and α_i are shown in Fig. 7. For a concentration of 23.7 vol%, three relaxation modes were obtained. The q dependences of Γ_i were $\Gamma_1 \propto q^{1.28}$ and $\Gamma_2 \propto q^{1.19}$ for the two slow modes, and Γ_3 had no clear q dependence for the fast mode (Fig. 7a). Note that the exponents of α_i ($i = 1, 2, 3$) should be regarded as $\alpha_i > 1$ although they approximately take 1 because α_i could be reduced by the effect of the particle size

polydispersity which was more than 20% even in the narrow-disperse systems as shown in Fig. 3. The behaviors of $\Gamma_i \propto q^n$ ($n < 2$) and $\alpha_i > 1$ ($i = 1, 2$) can be attributed to hyperdiffusive motions, which have been frequently observed in concentrated particle systems such as colloidal glasses and gels, due in part to a series of discrete rearrangement events.[46] On the other hand,

Γ_3, which is q-independent and much faster than the other two modes, may originate from a rotational diffusion, in reference to past studies for plate-like colloids.[36,37]

For 21.9 vol%, two different types of motion were observed. The faster dynamics (Γ_2) behaved as $\Gamma_2 \propto q^{4.85}$, $\alpha_2 < 1$ as shown in Fig. 7b. The behavior of $\Gamma_2 \propto q^n$ ($n > 2$) and $\alpha_2 < 1$ can represent the subdiffusive motions which have been observed in systems where particle motions are constrained.[47–50] On the other hand, the slower dynamics (Γ_1) behaved as $\Gamma_1 \propto q^{2.15}$, $\alpha_1 \sim 1$, representing almost simple diffusive motion. These behaviors are quite different from those for 23.7 vol%. The differences may arise from the increased inter-particle distance. As the inter-particle distance increases, the effect of the electrostatic interaction increases relative to the effect of excluded volume due to particle collisions. In such a situation, individual nanoplates can be trapped in cages, keeping a constant distance from the neighboring nanoplates under an electrostatic repulsive force. Such a cage effect based on inter-particle interactions suppresses diffusive motions of the particles, resulting in sub-diffusive behaviors.[48,50,51] The behaviors of the individual nanoplates changed from hyperdiffusive to subdiffusive dynamics when the concentration decreased from 23.7 to 21.9%, as with the case of a dense colloidal ellipsoid system.[34] The subdiffusive dynamical behavior observed at 18.8 vol%, $\Gamma_1 \propto q^{3.44}$, $\alpha_1 < 1$ (Fig. 7c), is also understood to be due to the effect of trapping by the electrostatic interactions. The change from hyperdiffusive to subdiffusive motion with increasing inter-particle distance might be universal in certain dense colloidal systems. There are only a few reported studies, and further investigation is needed.

The dynamics of anisotropic colloidal particles is governed by a complex interplay of factors such as particle shape, size, interparticle distance, excluded volume effects, electrostatic interactions, and hydrodynamic interactions. Despite the limited experimental data available on the dynamics of aniso-tropic particles, simulation studies have been vigorously conducted with the developing calculations of interparticle interactions.[29–31,52,53] Combined with findings from experiments and simulations, it would be possible to gain a deeper under-standing of anisotropic particle dynamics.

3   Conclusions

In conclusion, we have prepared $CaCO_3$ nanoplates with uniform thickness by a bio-inspired method using organic molecular templates combining SDS and PAA for 2D crystal growth of $CaCO_3$. The narrow-disperse nanoplates were isolated through size-fractionation using centrifugation. The POM and SAXS measurements revealed that the narrow-disperse nano-plates formed the N_C phase instead of the N_D phase without columnar structures. In the N_C phase, three distinct non-diffusive dynamics were clarified with the XPCS-based analyt-ical techniques combined with the Laplace transform for the designed colloidal liquid crystals with simpler and slower dynamics than molecular liquid crystals. These dynamical behaviors were analyzed in association with the relaxation rates, the q dependences of the relaxation rates, and the magnitudes
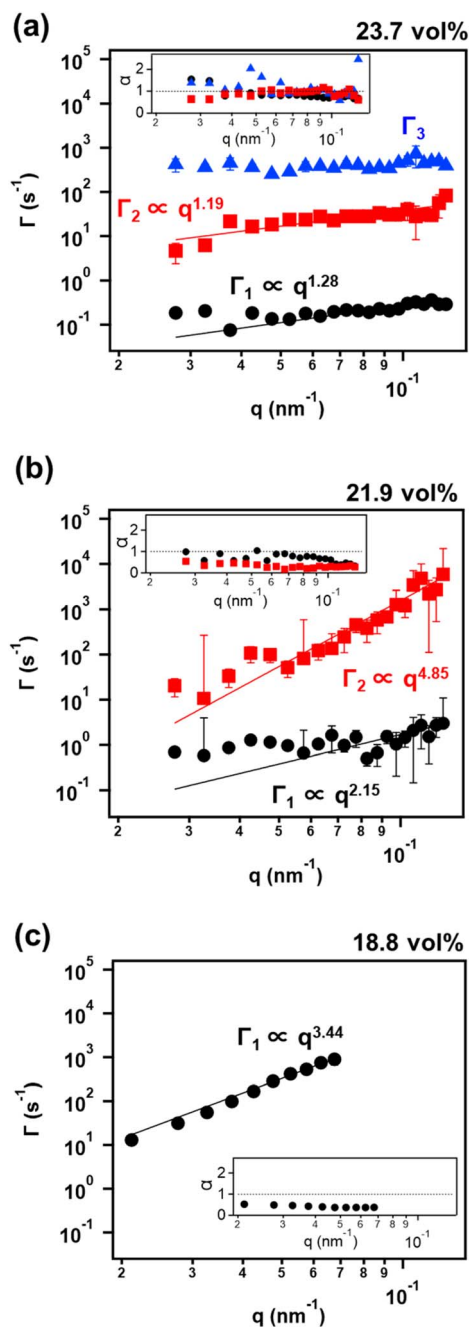

Fig. 7 XPCS analyses of the dynamics of N_C phases for narrow-disperse nanoplates. q dependences of relaxation rates Γ with the fitted curves for colloidal dispersions of narrow-disperse nanoplates at different concentrations of 23.7 vol% (a), 21.9 vol% (b), and 18.8 vol% (c). q dependences of exponents α are shown in the insets. Some of the downward error bars are omitted in 21.9 vol% (b) to avoid complicating the drawing.

of the stretched or compressed exponents. We believe that our experimental analyses will disclose underlying mechanisms in the dynamic and responsive phenomena of self-organized supramolecular columnar assemblies, contributing to their further functionalization.

4   Experimental

4.1   Synthesis of the nanoparticles

A 160 mM aqueous SDS (obtained from Wako) solution containing PAA ($M_W = 2.0 \times 10^3$, 2.9×10^{-1} wt%, obtained from Polysciences) was mixed with an equal volume of 200 mM aqueous $CaCl_2$ (obtained from Wako) solution. After 1 h of vigorous stirring of the mixed solution, an equal volume of 100 mM aqueous Na_2CO_3 (obtained from Kanto Chemical) solution was added, and the mixture was stirred for 5 days at room temperature. The resulting colloidal solution was filtered, and the residual precipitates were then centrifuged for 15 min at 10 000 rpm.

To remove excess salts, the precipitates were dispersed in an equal volume of 40 mM aqueous SDS solution and centrifuged again for 15 min at 10 000 rpm. Subsequently, an aqueous solution of 40 mM SDS was added to the precipitates to obtain colloidal dispersions of wide-disperse nanoplates with adjusted nanoplate concentrations.

The supernatant after collecting wide-disperse nanoplates was further centrifuged for 90 min at 10 000 rpm. Then, the sediment was dispersed in an equal volume of 40 mM aqueous SDS solution and centrifuged again for 90 min at 10 000 rpm. Finally, narrow-disperse nanoplates with adjusted nanoplate concentrations were obtained by addition of an aqueous solution of 40 mM SDS to the sediment.

4.2   Characterization of the nanoparticles

XRD patterns were recorded using a SmartLab (Rigaku) diffractometer with Cu Kα radiation. FTIR spectra were recorded on a Jasco FT/IR-6100 spectrometer (Jasco) with the KBr method. TG measurements (Rigaku, TG-8120) were performed up to 1000 °C at a heating rate of 10 °C min^{-1} under an air flow (100 mL min^{-1}). The optical properties of the samples were observed using a POM (Olympus, BX53). The crystal morphologies were examined using SEM (Hitachi, S-4700) after applying conductive treatment with a Hitachi E-1030 ion sputterer. Transmission electron microscope (TEM) observations were performed with a conventional TEM (JEOL, JEM-2000EX and JEM-2800, operated at 200 and 100 kV, respectively). The EDS analyses were conducted with a selected-area electron probe, for supporting grid free 2D templates and wide-disperse $CaCO_3$ nanoplates. Zeta potential measurements were conducted with a Zetasizer (Nano-ZS, from Malvern Instruments Ltd). UV-vis transmittance spectra were recorded using a JASCO FS-110 spectrometer.

4.3   X-ray scattering measurements

The SAXS and XPCS measurements were conducted on BL29XUL at SPring-8.[54] The undulator source and Si(111) monochromator were tuned to an energy of 12.40 keV and higher harmonic X-rays were removed using Pt-coated mirrors. The sample was irradiated with partially coherent X-rays obtained by passing the beam through 20 × 20 μm² slits. The scattered X-rays were detected using an EIGER 1 M 2D detector (Dectris, Switzerland) mounted approximately 6 m downstream of the sample. For X-ray scattering measurements, the samples were sealed in 10 μm-thick quartz capillary tubes with a diameter of 2 mm. All the X-ray scattering measurements were conducted after 2 or 3 days after sealing at room temperature.

The SAXS and XPCS data were obtained from the same sample and setup. The SAXS analysis of the static structure was performed from scattering images obtained with an exposure time of 1 s. On the other hand, the XPCS analysis of the dynamic behavior was performed by the time-resolved measurements of 10 000 frames with an exposure time of 1 ms.

Conflicts of interest

There are no conflicts to declare.

Acknowledgements

References

1 *Handbook of Liquid Crystals*, ed. J. W. Goodby, P. J. Collings, T. Kato, C. Tschierske, H. Gleeson and P. Raynes, Wiley-VCH, Weinheim, 2nd edn, 2014.

2 J. Uchida, B. Soberats, M. Gupta and T. Kato, *Adv. Mater.*, 2022, **34**, 2109063.

3 H. K. Bisoyi and Q. Li, *Chem. Rev.*, 2021, **122**, 4887–4926.

4 J. P. F. Lagerwall and G. Scalia, *Curr. Appl. Phys.*, 2012, **12**, 1387–1412.

5 T. Kato, J. Uchida, T. Ichikawa and T. Sakamoto, *Angew. Chem., Int. Ed.*, 2018, **57**, 4355–4371.

6 I. Dierking and S. Al-Zangana, *Nanomaterials*, 2017, **7**, 305.

7 T. Kato, M. Gupta, D. Yamaguchi, K. P. Gan and M. Nakayama, *Bull. Chem. Soc. Jpn.*, 2021, **94**, 357–376.

8 F. M. van der Kooij and H. N. W. Lekkerkerker, *J. Phys. Chem. B*, 1998, **102**, 7829–7832.

9 J. C. Gabriel, F. Camerel, B. J. Lemaire, H. Desvaux, P. Davidson and P. Batail, *Nature*, 2001, **413**, 504–508.

10 N. Miyamoto and T. Nakato, *Adv. Mater.*, 2002, **14**, 1267–1270.

11 Z. Xu and C. Gao, *Nat. Commun.*, 2011, **2**, 571.

12 J. E. Kim, T. H. Han, S. H. Lee, J. Y. Kim, C. W. Ahn, J. M. Yun and S. O. Kim, *Angew. Chem., Int. Ed.*, 2011, **50**, 3043–3047.

13 M. Nakayama, S. Kajiyama, T. Nishimura and T. Kato, *Chem. Sci.*, 2015, **6**, 6230–6234.

14 M. Nakayama, S. Kajiyama, A. Kumamoto, Y. Ikuhara and T. Kato, *Nanoscale Adv.*, 2020, **2**, 2326–2332.

15 M. Nakayama and T. Kato, *Acc. Chem. Res.*, 2022, **55**, 1796–1808.

16 M. Nakayama, S. Kajiyama, A. Kumamoto, T. Nishimura, Y. Ikuhara, M. Yamato and T. Kato, *Nat. Commun.*, 2018, **9**, 568.

17 S. Kajiyama, H. Iwase, M. Nakayama, R. Ichikawa, D. Yamaguchi, H. Seto and T. Kato, *Nanoscale*, 2020, **12**, 11468–11479.

18 M. Nakayama, W. Q. Lim, S. Kajiyama, A. Kumamoto, Y. Ikuhara, T. Kato and Y. Zhao, *ACS Appl. Mater. Interfaces*, 2019, **11**, 17759–17765.

19 L. A. Benedini, Y. Moglie, J. M. Ruso, S. Nardi and P. V. Messina, *Cryst. Growth Des.*, 2021, **21**, 2154–2166.

20 M. Sutton, *C. R. Phys.*, 2008, **9**, 657–667.

21 G. Grübel, A. Madsen and A. Robert, in *Soft Matter Characterization*, ed. R. Borsali and R. Pecora, Springer Netherlands, Dordrecht, 2008, pp. 954–995.

22 A. Madsen, R. L. Leheny, H. Guo, M. Sprung and O. Czakkel, *New J. Phys.*, 2010, **12**, 055001.

23 O. Bikondoa, X-Ray Photon Correlation Spectroscopy for the Characterization of Soft and Hard Condensed Matter, in *X-ray and Neutron Techniques for Nanomaterials Characterization*, ed. C. Kumar, Springer, Berlin, Heidelberg, 2016.

24 T. Hoshino, S. Fujinami, T. Nakatani and Y. Kohmura, *Phys. Rev. Lett.*, 2020, **124**, 118004.

25 C. H. Cheng, K. Kamitani, S. Masuda, K. Uno, N. Dechnarong, T. Hoshino, K. Kojio and A. Takahara, *Polymer*, 2021, **229**, 124003.

26 T. Hoshino, Y. Okamoto, A. Yamamoto and H. Masunaga, *Sci. Rep.*, 2021, **11**, 9767.

27 B. M. Yavitt, L. Wiegart, D. Salatto, Z. Huang, L. Tsapatsaris, M. K. Endoh, S. Poeller, M. Schiel, S. Petrash and T. Koga, *ACS Appl. Eng. Mater.*, 2023, **1**, 868–876.

28 T. Hoshino, M. Nakayama, S. Fujinami, T. Nakatani, Y. Kohmura and T. Kato, *Soft Matter*, 2019, **15**, 3315–3322.

29 A. Patti, D. El Masri, R. van Roij and M. Dijkstra, *Phys. Rev. Lett.*, 2009, **103**, 248304.

30 A. Patti, S. Belli, R. van Roij and M. Dijkstra, *Soft Matter*, 2011, **7**, 3533.

31 N. Morillo, A. Patti and A. Cuetos, *J. Chem. Phys.*, 2019, **150**, 204905.

32 A. S. Poulos, D. Constantin, P. Davidson, B. Pansu, E. Freyssingeas, A. Madsen and C. Chaneac, *J. Chem. Phys.*, 2010, **132**, 091101.

33 A. Pal, V. A. Martinez, T. H. Ito, J. Arlt, J. J. Crassous, W. C. K. Poon and P. Schurtenberger, *Sci. Adv.*, 2020, **6**, eaaw9733.

34 A. Pal, M. A. Kamal, P. Holmqvist and P. Schurtenberger, *Phys. Rev. Res.*, 2021, **3**, 023254.

35 D. Constantin, P. Davidson, E. Freyssingeas and A. Madsen, *J. Chem. Phys.*, 2010, **133**, 224902.

36 D. Kleshchanok, M. Heinen, G. Nägele and P. Holmqvist, *Soft Matter*, 2012, **8**, 1584–1592.

37 P. Holmqvist, V. Meester, F. Westermeier and D. Kleshchanok, *J. Chem. Phys.*, 2013, **139**, 084905.

38 G. Sakane, M. Tomohara, Y. Katayama and K. Hayashi, *Acta Crystallogr., Sect. E: Struct. Rep. Online*, 2010, **66**, m749.

39 M. C. Mourad, D. V. Byelov, A. V. Petukhov, D. A. Matthijs de Winter, A. J. Verkleij and H. N. Lekkerkerker, *J. Phys. Chem. B*, 2009, **113**, 11604–11613.

40 P. Davidson, C. Penisson, D. Constantin and J. P. Gabriel, *Proc. Natl. Acad. Sci. U. S. A.*, 2018, **115**, 6662–6667.

41 M. Zeng, D. King, D. Huang, C. Do, L. Wang, M. Chen, S. Lei, P. Lin, Y. Chen and Z. Cheng, *Proc. Natl. Acad. Sci. U. S. A.*, 2019, **116**, 18322–18327.

42 F. Chaput, F. Lerouge, A.-L. Bulin, D. Amans, M. Odziomek, A.-C. Faure, M. Monteil, I. Dozov, S. Parola, F. Bouquet, M. Lecouvey, P. Davidson and C. Dujardin, *Langmuir*, 2019, **35**, 16256–16265.

43 K. Kanie, T. Yasuda, M. Nishii, S. Ujiie and T. Kato, *Chem. Lett.*, 2001, **30**, 480–481.

44 B. J. Berne and R. Pecora, *Dynamic light scattering: with applications to chemistry, biology, and physics*, Wiley, New York, 1976.

45 S. W. Provencher, *Comput. Phys. Commun.*, 1982, **27**, 229–242.

46 L. Cipelletti and L. Ramos, *J. Phys.: Condens. Matter*, 2005, **17**, R253–R285.

47 A. Duri and L. Cipelletti, *Europhys. Lett.*, 2006, **76**, 972–978.

48 J. Sprakel, J. van der Gucht, M. A. Cohen Stuart and N. A. Besseling, *Phys. Rev. Lett.*, 2007, **99**, 208301.

49 C. Caronna, Y. Chushkin, A. Madsen and A. Cupane, *Phys. Rev. Lett.*, 2008, **100**, 055702.

50 T. Hoshino, D. Murakami, Y. Tanaka, M. Takata, H. Jinnai and A. Takahara, *Phys. Rev. E: Stat., Nonlinear, Soft Matter Phys.*, 2013, **88**, 032602.

51 E. R. Weeks and D. A. Weitz, *Chem. Phys.*, 2002, **284**, 361–367.

52 C. De Michele, R. Schilling and F. Sciortino, *Phys. Rev. Lett.*, 2007, **98**, 265702.

53 R. Yamamoto, J. J. Molina and Y. Nakayama, *Soft Matter*, 2021, **17**, 4226–4253.

54 K. Tamasaku, Y. Tanaka, M. Yabashi, H. Yamazaki, N. Kawamura, M. Suzuki and T. Ishikawa, *Nucl. Instrum. Methods Phys. Res., Sect. A*, 2001, **467**, 686–689.